Hindawi
International Journal of Antennas and Propagation
Volume 2022, Article ID 1320284, 10 pages
https://doi.org/10.1155/2022/1320284

Research Article

Coplanar Discontinuous Transmission Line Feed for Phase Gradient Metasurface Antenna

Yiying Wang,[1,2] Xianxi Wu,[1,2] Yuntao Yan,[3] Jianfeng Wan,[2] Jinjun Mo,[1,2] Yannan Jiang,[1,2] and Xinhua Yu[1,2]

[1]*Guangxi Key Lab of Wireless Wideband Communication and Signal Processing, Guilin 541000, China*
[2]*Guilin University of Electronic Technology, Guilin 541000, China*
[3]*Xi'an Electronic Engineering Research Institute, Xi'an 710000, China*

Correspondence should be addressed to Xinhua Yu; yusilian@126.com

Received 25 May 2022; Accepted 20 August 2022; Published 21 October 2022

Academic Editor: Chien-Jen Wang

The aim of this study is to efficiently excite the radiation of phase gradient metasurface (PGM), a novel coplanar discontinuous transmission line feed is proposed for reduction of the profile, where 12 uniform discontinuous rectangular rings form the feeding structure. The unit cells of PGM are symmetrically placed on both sides of this feed structure at the same layer, and they are close enough. The measurements agree well with those of simulations in the range of 10.48–11.18 GHz.

1. Introduction

The Phase Gradient Metasurface (PGM), as one type of 2D pattern metamaterial [1], has been widely used in many applications, such as near-field meta-steering systems [2], far-field subwavelength imaging [3], radar system, and satellite communication [4]. The researchers employed the PGM to enhance the antenna performance. In [5–7], the authors placed patch antennas on the focuses of PGM to improve the gain or bandwidth, and it can be made into a dome in a similar way to increase the scan range for the phased array [8, 9]. It is also used to adjust RCS. Literature [4, 10, 11] reduced the RCS depending on its inherent property of anomalous reflection and diffuse reflection, while [12] redirected the scattering dispersed by the conducting cylinder to produce effective retroreflection for the enhancement of RCS. And controlling the beam by means of PGM was realized as well. The p-i-n diodes were used to tune the PGM in order to steer the radiation beam in [4], while this was done by rotating the PGM in [13]. The two radiation beams at two different frequencies were realized by the excitation of the horn antenna on the PGM [14]. On the contrary, the multibeams radiation was got through the coding sequence, where they used different codes to control the different radiation beams [15].

On the other side, the PGM can be used to radiate directly, that's the PGM antenna, and many feeding techniques have been adopted [16–21]. Literature [16] showed a feed of elaborately-designed waveguide to excite the PGM next to it for the in-plane feed antenna design, and the modified parallel-plate-like waveguide feed structure was designed in [17], where both feeds are higher than those of PGM cells. In contrast, the authors put the PGM on the spoof surface plasmon polariton (SSPP) for its radiation, and the rectangular waveguide [18] and the monopole antenna with both metal wall and metallic grooves [19] to excite SSPP were designed, respectively. Additionally, the authors in [20] designed a vertical corrugated metallic strip to excite the parallel symmetrical placed PGM unit cells directly. To reduce the profile, the 2D feed antenna structure was studied in [21, 22]. In [21], the parallel plate waveguide feed was adopted which is on the same layer as PGM and then excites the front unit cells, while the coplanar waveguide was employed to excite SSPP, and then, convert the surface plasmon polariton (SPP) mode to the radiated mode with the help of PGM [22].

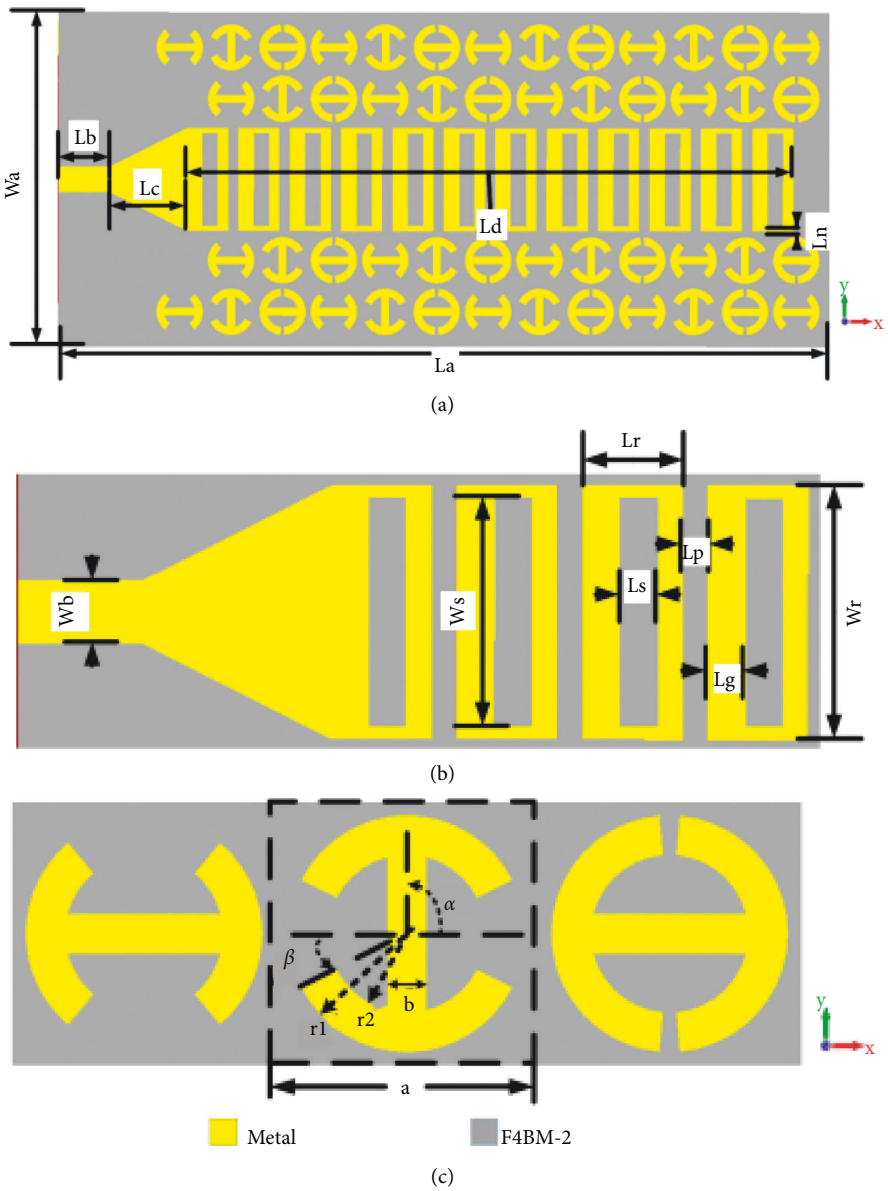

Figure 1: Antenna configuration. (a) Top view. (b) Feed structure. (c) PGM cell.

We have found the suspended microstrip line feed connected with a conventional rectangular waveguide [23] and the slotted rectangular cavity feed [24] to excite PGM efficiently. However, the profiles are high. Thus, a novel feed structure is proposed for the planar design in the application of efficient energy collector, where the feed structure is taken on the same layer as PGM. The feed resembles the conventional microstrip line placed on the substrate but consists of 12 discontinuous rectangular rings with constant spacing. The first ring gets power from the conventional microstrip line, while the rest is obtained by mutual coupling. Then, two rows of PGMs are put symmetrically on both sides, and they are close enough for the effective radiation of PGMs.

2. Antenna Design

The whole antenna configuration is shown in Figure 1, where Figure 1(a) is the top view of the antenna, including the feed structure and the corresponding PGMs, while (b) and (c) present the detailed designs for the planar feed structure and the unit cells of one period, respectively. It is clear that the feed structure and the PGMs are placed on the same layer, the PGMs were close enough to the feed and to get the effective coupling for their radiations and two rows of PGMs are designed to enhance the realized gain. In this antenna, the F4BM-2 is used as the substrate whose height is 3 mm and the corresponding permittivity and loss tangent are 2.65 and 0.0015, respectively. Here, the ground plane layer is not

shown in the figure, because it's right under the substrate and composed of the whole metal. The gold color represents the metal while the grey is of the substrate. The detailed designs for the planar feed structure and unit cells of one period of PGM are discussed as follows.

2.1. Feed Configuration. Figure 1 depicts the planar feed structure placed in the middle of PGMs. It is similar to the conventional microstrip line, but the transmission line is sliced into 12 discontinuous rectangular rings, and they obtain power by coupling from the previous adjacent ring. And a transition section is designed to connect the regular rectangular microstrip line, which will be connected with an SMA connector in the test antenna. Figure 1(b) shows the detailed design of the planar feed structure, including the narrow microstrip line, the transition microstrip line and the discontinuous rings. In addition, the corresponding variables involved in this feed design are indicated in these two subfigures.

The width and length of the antenna are represented by variables Wa and La, respectively, which are determined by the intended antenna performance for the efficient energy collector application. The variables of feed involves the width Wb and length Lb of regular microstrip line, the length Lc of transition section, and those of discontinuous ring, including the interval length Lp, the length Ls and width Ws of the slot of the ring, the length Lr of ring and the width Lg of the left arm. In order to get enough coupling power from the discontinuous microstrip line; two key distance variables are indicated in Figure 1(a). They are the distance Ln between the discontinuous microstrip line and the unit cell of PGMs.

The Wb equals 5.0 mm in order to assure that the characteristic impedance of the microstrip line is 50Ω, and the length Lc is used to adjust the match between the microstrip lines and rings. The variable Lp affects the mutual coupling of the rings definitely, and it should be small enough, while the Ln should be small as well in order to excite the PGMs effectively. On the contrary, Wr and Lr determine the resonant frequency of this ring, where the perimeter of the ring is equal to one wavelength of 10.5 GHz. The final values of the mentioned variables of feed structure are listed in Table 1.

2.2. Design of PGM. The "I"-shaped unit cell is selected to be the radiators whose design method is the same as in [9, 10] and shown in Figure 1(c). There are three unit cells to form the phase gradient with a difference of 120°.

There are several variables to be considered in this design, as indicated in Figure 1(c). The α is the angle between the power propagation direction and the center of the strip of cell, which is set to be 0° for wideband design. While the angle β corresponds to the open angle for the split resonant ring. And the radius of the split resonator $r1$ and $r2$ belongs to those of outer and inner circles, respectively. The rest variables are period a, and width b, which determines the corresponding inductance and capacitance and are kept constant for this cell.

Table 1: The values of feed structure (unit: mm).

Parameter	Value
Wa	65.0
La	150.0
Wb	5.0
Lb	18.0
Ws	18.0
Ls	3.0
Wn	22.4
Wr	20.0
Lr	8.0
Lc	15.0
Ld	118.0
Lg	3.0
Lp	3.0
Ln	1.2

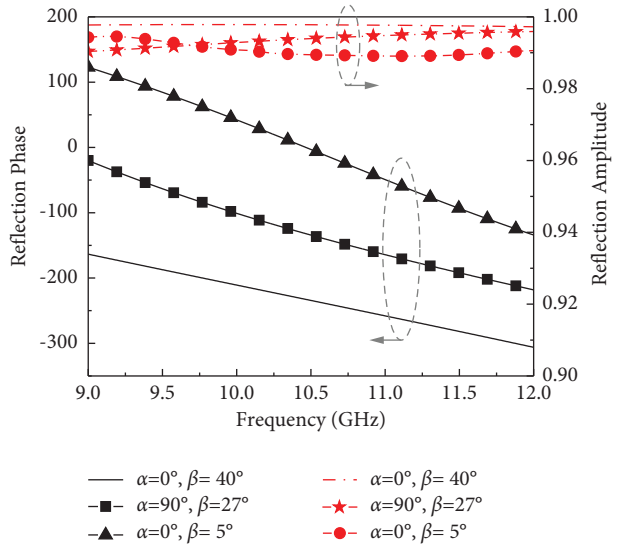

Figure 2: Reflective phases and amplitudes of the PGM.

According to the intended resonant frequency of 10.5 GHz, the calculated values for the aforementioned variables are $a = 10$ mm, $r1 = 4.5$ mm, $r2 = 3$ mm, and $b = 1.5$ mm. Meanwhile, the final optimized values for these three unit cells are (0°, 40°), (90°, 27°), and (0°, 5°), respectively. Their reflective phase and amplitude are shown in Figure 2. In the concerning bandwidth, the amplitudes are greater than 0.99 while the phase difference of adjacent cells is 120°.

3. Result Analysis

The unit cells of the outer row are put close to the inner ones with a distance of 1.0 mm and have one cell more than those of the inner row so as to couple power and radiate effectively. Consequently, the corresponding result analyses are done as follows: parametric analysis, PGM radiation, reflection coefficient, realized gain, and radiation patterns.

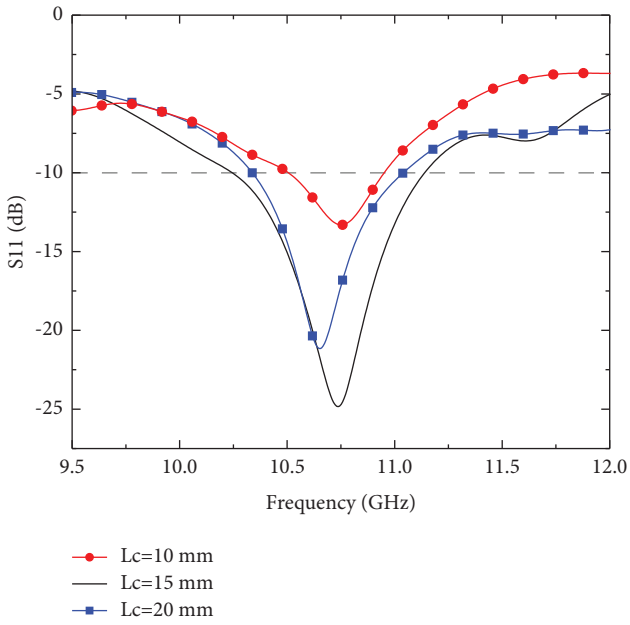

Figure 3: Parametric analysis for the length *Lc* of transition section.

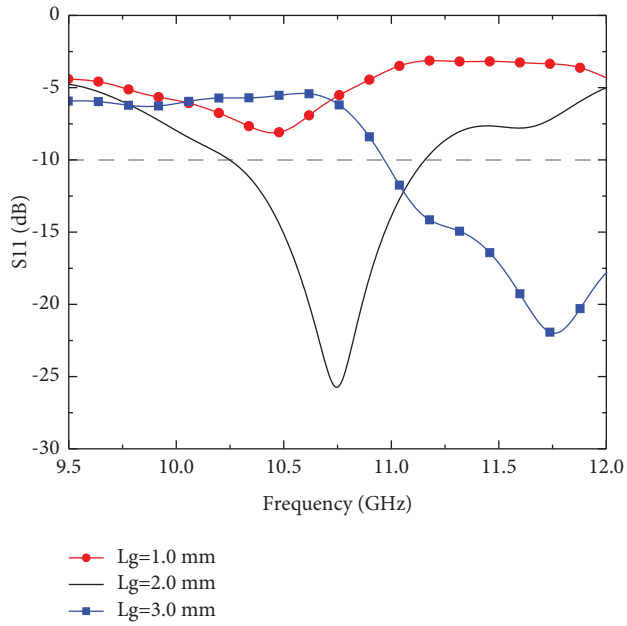

Figure 4: Parametric analysis for the width *Lg* of feed structure.

3.1. Parametric Analysis of Feeding Structure. As aforementioned, all the parameters affect the final result of the antenna. However, we just choose the key ones to analyse their influences to the antenna performance, where only the selected variable changes while the others are kept as constants. They are, (1) the length *Lc* of transition area to adjust the matching, (2) the width *Lg* of the left metal of the loop, which corresponds to the width of spacing *Ls* and affects the metal area of rectangular loop, (3) the spacing *Lp* between adjacent loops who determines the coupling, and (4) the distance *Ln* between the PGM and the loop which involves the power coupling for the PGM.

The parametric analysis of *Lc* to S11 is shown in Figure 3, where the black line is the final optimized value, and the red line with circles and the blue line with rectangles are the results of lower and higher values, respectively. The width *Wr* is kept as a constant in this process so that the parameter *Lc* affects the open angle of transition area, and influences the matching frequency and bandwidth as well. It is clear in this figure that the matching becomes better as *Lc* increases from 10 mm to 15 mm and the resonant frequency shifts to the lower, but the bandwidth narrows when the value is higher than 15 mm and the matching turns worse.

The change of parameter *Lg* will lead to the change of *Ls* immediately because both determine the metal area of rectangular loop. Its influence on the S11 is shown in Figure 4, from where we know that we have to define this parameter carefully owing to it not only affects the matching but also the resonance. And it is one of the key parameters to determine the final S11.

We depict the parametric analysis of *Lp* in Figure 5. It mainly affects the resonance, where the resonance shifts to a higher frequency as it increases, while the bandwidth is almost kept as constant in the process of change. Furthermore, the matching becomes worse but still remains in a good matching level near the concerning bandwidth.

The parameter *Ln* indicates the distance between the unit cell and the feed structure, and it determines the coupling to the PGM and the final radiation power. The effect on the S11 is shown in Figure 6. It is clear that when Ln is less than the optimized value 1.2 mm, there is almost no effect to the S11, including the matching, resonance, and bandwidth. Even it becomes to be a very large value that is 6.2 mm which has 5.0 mm difference from the optimized 1.2 mm, the matching and resonance are almost no change except the bandwidth widens.

In one word, the parameters of the feeding structure, that is the proposed discontinuous transmission line, affect the final S11 of the antenna, while the distance Ln just influences the coupling for the radiation power.

3.2. Verification of Radiation of PGM. The discontinuous rings can radiate into free space owing to the mutual coupling to realize the power propagation on the transmission line. Additionally, the rings are a potential radiation source as well. The corresponding current distribution and 3D radiation pattern at 10.5 GHz without consideration of PGM are shown in Figures 7(a) and 7(b), whereas the radiation with PGM is shown in Figure 7(c).

From Figure 7(a), the power propagation on the transmission line is very clear that the ring gets power by coupling from the previous neighbouring one, and the current flows in reverse. The current in the ring is reversed as well. These result in radiations caused by the discontinuous transmission line. This phenomenon is indicated in Figure 7(b) where the maximum direction is along the direction of the discontinuous line. When the PGM is put beside the feed structure, its radiation dominates and concentrates the radiation to a fixed area whose direction is almost vertical to the transmission line. The corresponding 3D pattern in Figure 7(c) shows this directional radiation.

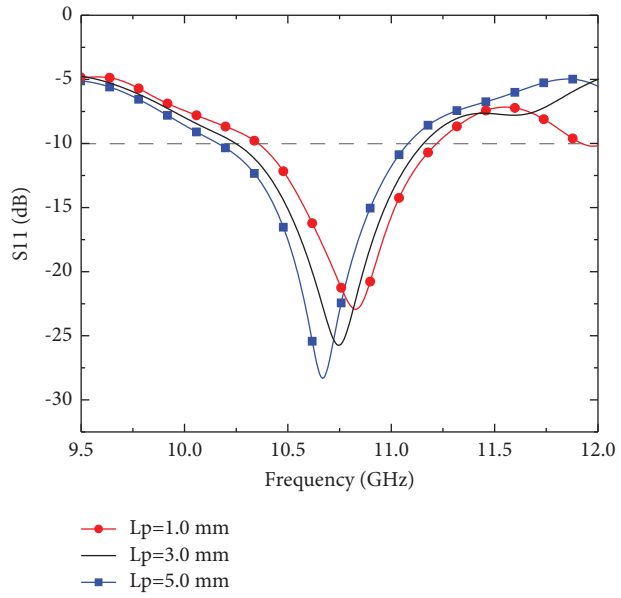

Figure 5: Parametric analysis for the width *Lp* of feed structure.

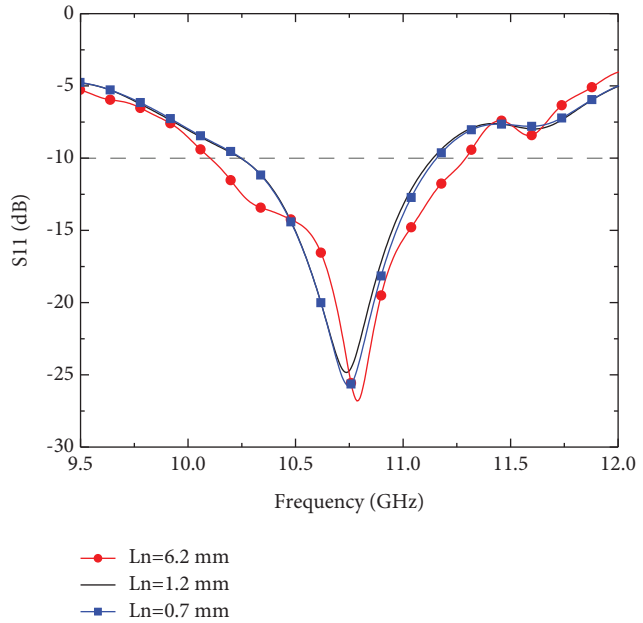

Figure 6: Parametric analysis for the width *Ln* of feed structure.

3.3. S11 and Realized Gain. The antenna prototype is fabricated and measured in the anechoic chamber, and the corresponding results of S11 and realized gain are compared. These are shown in Figure 8, where (a) presents the antenna prototype without connecting with the SMA connector, (b) is the measurement situation in an anechoic chamber, and (c) and (d) are the comparisons of simulated and measured S11s and realized gains, respectively.

The measured results are indicated by the black solid lines with squares in Figures 8(c) and 8(d), while the simulations are represented by the red lines with circles. The two comparisons show that the measured results agree well with those of the simulated. The measured resonant frequency is 10.8 GHz, which shifts a little to a higher frequency than the intended 10.5 GHz. The measured bandwidth becomes narrower than the simulated result, which 700 MHz is ranging from 10.48 GHz to 11.18 GHz, while the simulated bandwidth is 900 MHz from 10.25 GHz to 11.15 GHz. However, the matching is almost the same. Figure 8(d) indicates that the difference between the measured and the simulated realized gains are less than 1 dB which validates the feed design.

3.4. Pattern Comparison. As we all know that the radiation of PGM has the frequency scanning property. Thus, the comparisons of E-plane patterns at four different

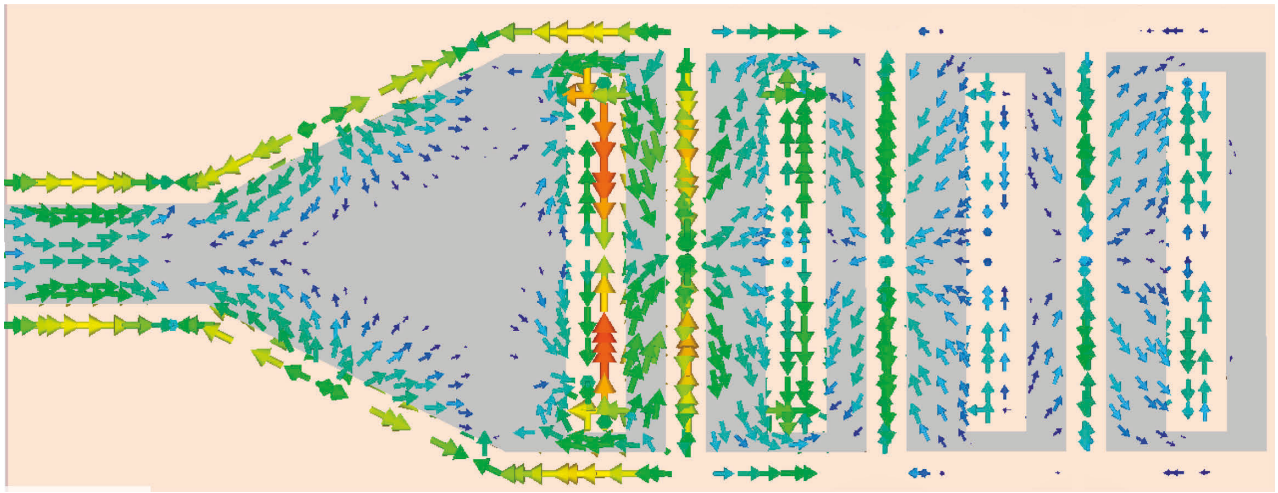

(a)

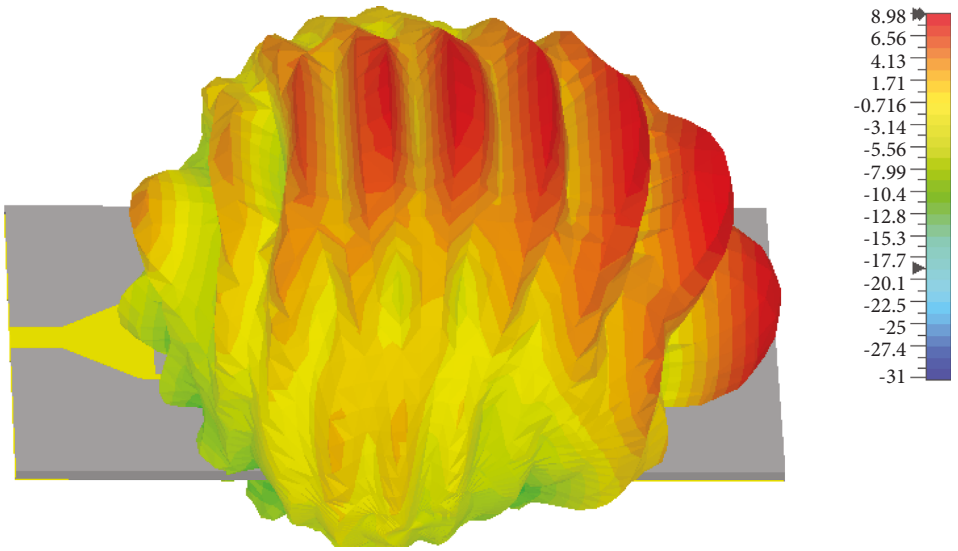

(b)

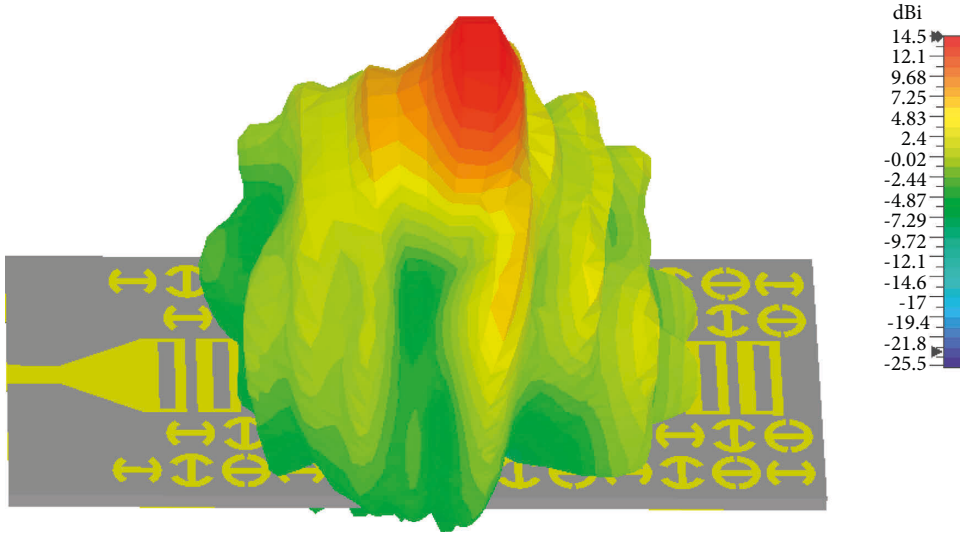

(c)

Figure 7: (a) Current distribution. (b) 3D patterns without PGM. (c) 3D patterns with PGM.

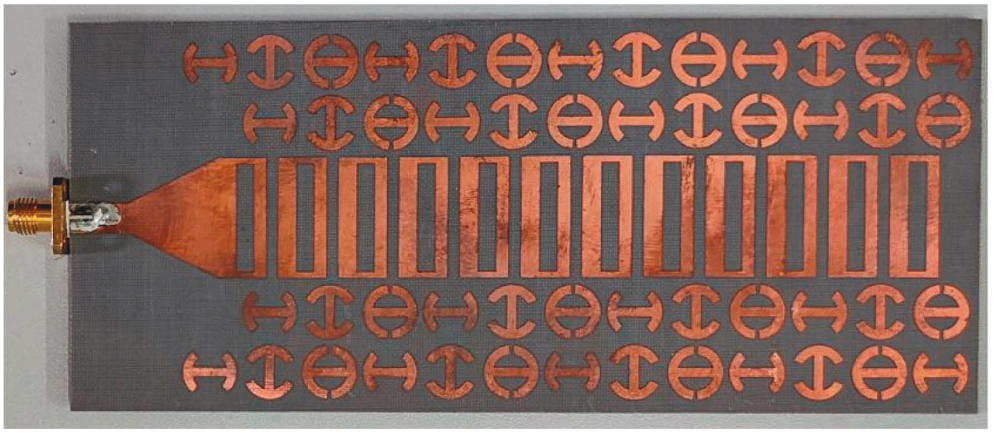

(a)

(b)

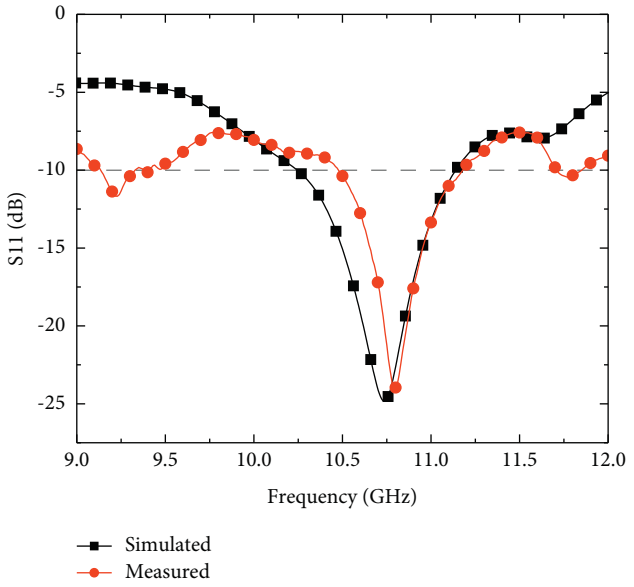

(c)

Figure 8: Continued.

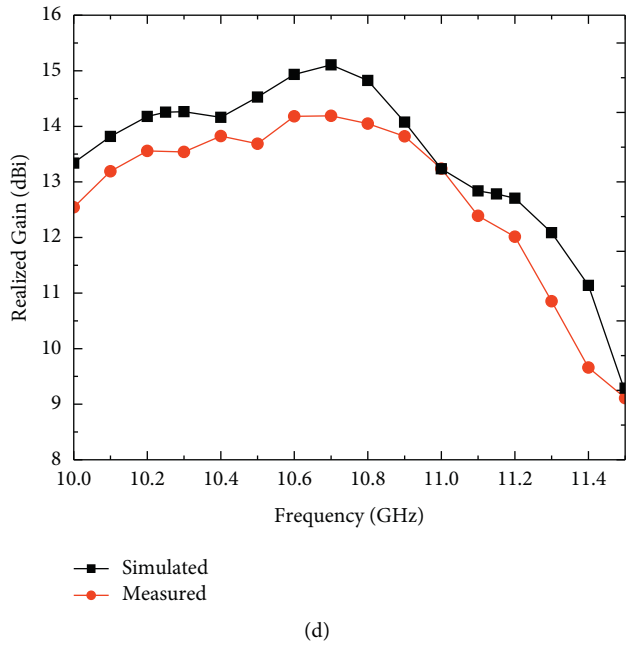

Figure 8: Measurement and comparisons. (a) Antenna prototype. (b) Measurement in anechoic chamber. (c) S11 comparison. (d) Realized gain comparison.

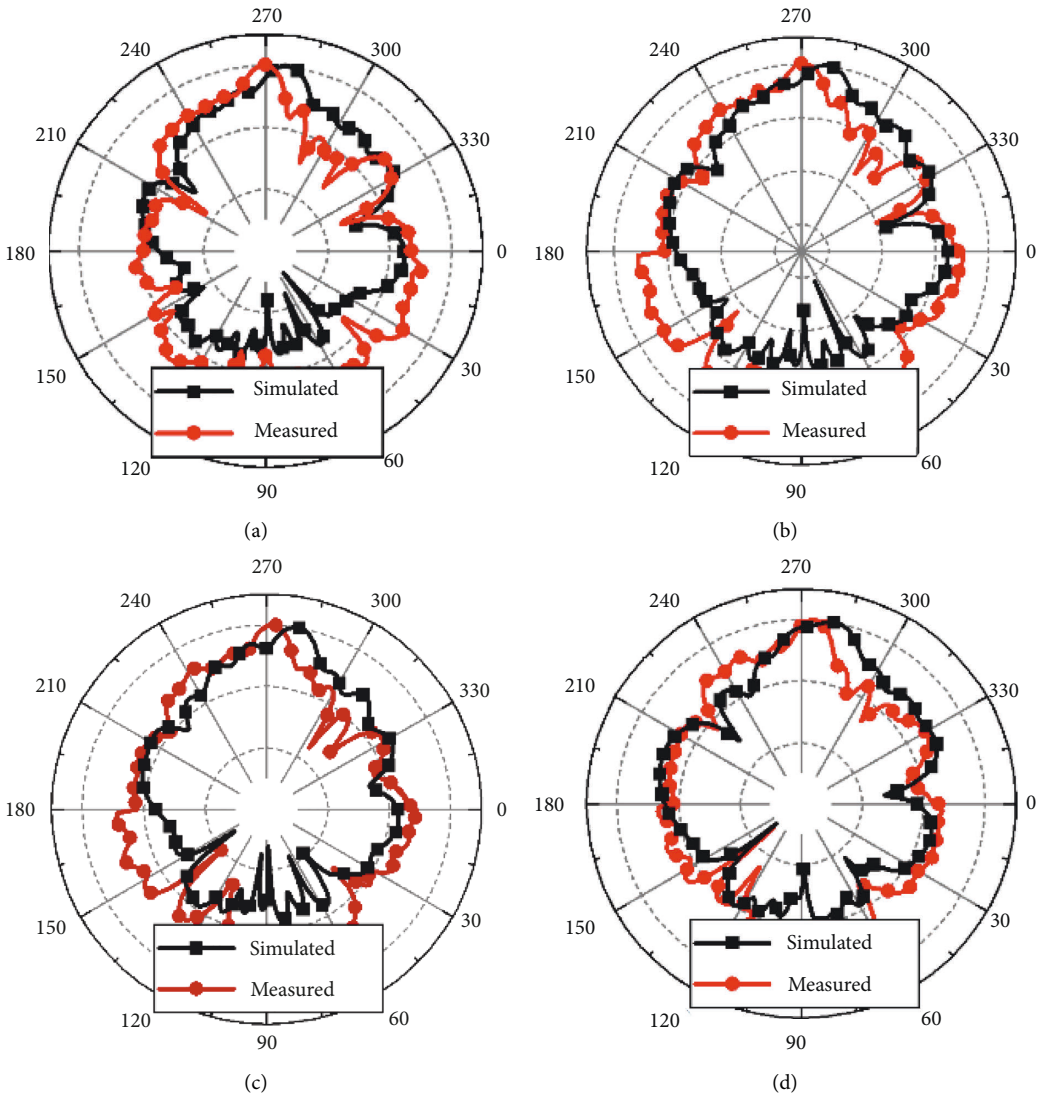

Figure 9: E-plane pattern comparisons. (a) 10.3 GHz. (b) 10.5 GHz. (c) 10.7 GHz. (d) 11.1 GHz.

frequencies in the bandwidth are shown in Figure 9, where 10.3 GHz, 10.5 GHz, 10.7 GHz, and 11.1 GHz are chosen to be compared. The black solid lines with squares represent the simulated results and the red lines with circles belong to the measurements.

The tilt angles are different from those of simulations, this is because the antenna under test was not aligned with the transmitted antenna, and this is also the reason that the measured realized gains are 1 dB less than those of simulations in the concerning bandwidth. However, the maximum radiations of simulations appear at 7°, 8°, 9°, and 10° for the above four frequencies, respectively.

4. Conclusions

In order to reduce the profile of the radiation of PGM, a novel planar discontinuous transmission line feed was proposed. It consists of 12 uniform discontinuous rectangular rings, and the PGM cells are put beside the feed. The first ring is fed by the microstrip line; the following ring gets power by coupling the previous neighbouring one, and then, forms the power propagation on them. Two rows of "I"-shaped PGM cells were designed and placed symmetrically to the feed. Finally, the antenna prototype was fabricated and measured where the measurements agreed well with the simulations.

Data Availability

The data used to support the findings of this study are included within the article.

Conflicts of Interest

The authors declare that they have no conflicts of interest.

Acknowledgments

This work was supported by the Natural Science Foundation of Guangxi under Grants 2019GXNSFFA245002; Guangxi Key Laboratory of Wireless Wideband Communication and Signal Processing under Grants GXKL06200101, GXKL06180104, GXKL06200111 and GXKL06190118; and National Natural Science Foundation of China under Grant 12161025; and National Key Laboratory of Science and Technology on Test Physics and Numerical Mathematics of China under Grant no. HTKJ2020KL014003.

References

[1] C. L. Holloway, E. F. Kuester, J. A. Gordon, J. O'Hara, J. Booth, and D. R. Smith, "An overview of the theory and applications of metasurfaces: the two-dimensional equivalents of metamaterials," *IEEE Antennas and Propagation Magazine*, vol. 54, no. 2, pp. 10–35, 2012.

[2] K. Singh, M. U. Afzal, and K. P. Esselle, "Designing efficient phase-gradient metasurfaces for near-field meta-steering systems," *IEEE Access*, vol. 9, pp. 109080–109093, 2021.

[3] P. Salami and L. Yousefi, "Far-field subwavelength imaging using phase gradient metasurfaces," *Journal of Lightwave Technology*, vol. 37, no. 10, pp. 2317–2323, 2019.

[4] J. Yu, W. Jiang, and S. Gong, "Low-RCS beam-steering antenna based on reconfigurable phase gradient metasurface," *IEEE Antennas and Wireless Propagation Letters*, vol. 18, no. 10, pp. 2016–2020, 2019.

[5] H. Li, G. Wang, H. X. Xu, T. Cai, and J. Liang, "X-band phase-gradient metasurface for high-gain lens antenna application," *IEEE Transactions on Antennas and Propagation*, vol. 63, no. 11, pp. 5144–5149, 2015.

[6] H. Li, G. Wang, J. Liang, X. Gao, H. Hou, and X. Jia, "Single-layer focusing gradient metasurface for ultrathin planar lens antenna application," *IEEE Transactions on Antennas and Propagation*, vol. 65, no. 3, pp. 1452–1457, 2017.

[7] J. J. Liang, G. L. Huang, J. N. Zhao, Z. J. Gao, and T. Yuan, "Wideband phase-gradient metasurface antenna with focused beams," *IEEE Access*, vol. 7, pp. 20767–20772, 2019.

[8] A. Benini, E. Martini, S. Monni et al., "Phase-gradient metadome for increasing grating-lobe-free scan range in phased arrays," *IEEE Transactions on Antennas and Propagation*, vol. 66, no. 8, pp. 3973–3982, 2018.

[9] Y. H. Lv, X. Ding, B. Z. Wang, and D. E. Anagnostou, "Scanning range expansion of planar phased arrays using metasurfaces," *IEEE Transactions on Antennas and Propagation*, vol. 68, no. 3, pp. 1402–1410, 2020.

[10] W. Zhang, Y. Liu, S. Gong, J. Wang, and Y. Jiang, "Wideband RCS reduction of a slot array antenna using phase gradient metasurface," *IEEE Antennas and Wireless Propagation Letters*, vol. 17, no. 12, pp. 2193–2197, 2018.

[11] Y. Fan, J. Wang, Y. Li et al., "Low-RCS multi-beam metasurface-inspired antenna based on pancharatnam – berry phase," *IEEE Transactions on Antennas and Propagation*, vol. 68, no. 3, p. 1899, 1906.

[12] Y. Shang and Z. Shen, "Polarization-independent backscattering enhancement of cylinders based on conformal gradient metasurfaces," *IEEE Transactions on Antennas and Propagation*, vol. 65, no. 5, pp. 2386–2396, 2017.

[13] K. Singh, M. U. Afzal, M. Kovaleva, and K. P. Esselle, "Controlling the most significant grating lobes in two-dimensional beam-steering systems with phase-gradient metasurfaces," *IEEE Transactions on Antennas and Propagation*, vol. 68, no. 3, pp. 1389–1401, 2020.

[14] H. Yue, L. Chen, Y. Yang, L. He, and X. Shi, "Design and implementation of a dual frequency and bidirectional phase gradient metasurface for beam convergence," *IEEE Antennas and Wireless Propagation Letters*, vol. 18, no. 1, pp. 54–58, 2019.

[15] H. Wang, Y. Li, H. Chen et al., "Multi-beam metasurface antenna by combining phase gradients and coding sequences," *IEEE Access*, vol. 7, pp. 62087–62094, 2019.

[16] Ya Fan, J. Wang, H. Ma et al., "In-plane feed antennas based on phase gradient metasurface," *IEEE Transactions on Antennas and Propagation*, vol. 64, no. 9, pp. 3760–3765, 2016.

[17] X. Liu, B. Chen, J. Zhang et al., "Frequency-scanning planar antenna based on spoof surface plasmon polariton," *IEEE Antennas and Wireless Propagation Letters*, vol. 16, pp. 165–168, 2017.

[18] H. Chen, H. Ma, Y. Li et al., "Wideband frequency scanning spoof surface plasmon polariton planar antenna based on transmissive phase gradient metasurface," *IEEE Antennas and Wireless Propagation Letters*, vol. 17, no. 3, pp. 463–467, 2018.

[19] D. Wang, G. Wang, T. Cai et al., "Planar spoof surface plasmon polariton antenna by using transmissive phase

gradient metasurface," *Annalen der Physik*, vol. 532, no. 6, pp. 2000008–2000017, 2020.

[20] Y. Fan, J. Wang, Y. Li et al., "Frequency scanning radiation by decoupling spoof surface plasmon polaritons via phase gradient metasurface," *IEEE Transactions on Antennas and Propagation*, vol. 66, no. 1, pp. 203–208, 2018.

[21] B. Li, X. Liu, H. Shi, C. Yang, Q. Chen, and A. Zhang, "Planar phase gradient metasurface antenna with low RCS," *IEEE Access*, vol. 6, pp. 78839–78845, 2018.

[22] J. J. Xu, H. C. Zhang, Q. Zhang, and T. J. Cui, "Efficient conversion of surface-plasmon-like modes to spatial radiated modes," *Applied Physics Letters*, vol. 106, no. 2, pp. 021102–021106, 2015.

[23] X. Yu, X. Wu, W. Shao, G. Cheng, and Y. Wang, "High-gain radiation of phase gradient metasurface using parallel-plate-like feed," in *Proceedings of the 2021 Int. Conf. Microw. Millim. Wave Technol. ICMMT 2021 - Proc*, pp. 2021–2023, Nanjing, China, May 2021.

[24] X. Yu, G. Sun, J. Wan et al., "Rectangular-cavity-like feed for radiation of phase gradient metasurface," *Microwave and Optical Technology Letters*, vol. 63, no. 12, pp. 2927–2932, 2021.